Stepwise allomorphic transformations by alkaline and ethylenediamine treatments on bamboo crystalline cellulose for enhanced enzymatic digestibility

Zhe Ling[a], Wei Tang[a], Yan Su[a], Caoxing Huang[a], Chenhuan Lai[a], Alex Kirui[b], Tuo Wang[b], Alfred D. French[c], Qiang Yong[a,*]

[a] Jiangsu Co-Innovation Center of Efficient Processing and Utilization of Forest Resources, College of Chemical Engineering, Nanjing Forestry University, Nanjing 210037, China

[b] Department of Chemistry, Louisiana State University, Baton Rouge, LA 70803, USA

[c] Southern Regional Research Center, Agricultural Research Service, USDA, New Orleans, LA 70124, USA

*Corresponding author: Qiang Yong

E-mail: swhx@njfu.com.cn

ABSTRACT: Efficient modification and decrystallization of cellulose Iβ in lignocellulosic biomass are potential ways to overcome biomass recalcitrance and facilitates enzymatic degradation. Herein, we have treated moso bamboo and microcrystalline cellulose separately by either alkali or ethylenediamine (EDA) treatments, as well as using both in succession. The pretreatments successfully transformed the initial cellulose Iβ allomorph into cellulose II, III_I, and cellulose III_{II}. Crystal structures and crystallinities were determined by Rietveld X-ray diffraction and CP/MAS ^{13}C NMR. Comparatively, the samples that were sequentially treated by EDA and NaOH had low crystallinity (~50%), larger d-spacings of ~4.4 Å for the hydrophobic (110) planes, and less condensed microfibrillar aggregation. The factors simultaneously contributed to as high enzymatic hydrolysis yield as 89.5% and 91.7% respectively, followed by the yields of mercerized cellulose II and cellulose III_{II} allomorph. The stepwise allomorphic transformations may provide new strategies on improving efficiency of saccharification process and biomass utilization.

Keywords: crystalline cellulose; stepwise pretreatment; allomorphic transformation; cellulose III_{II}; biorefinery

1. Introduction

The efficient conversion of cellulose to fermentable sugars by cellulase enzyme-catalysis has been receiving considerable attention and is making important contributions to the development of a sustainable society (Mosier et al., 2002). Native cellulose is a linear polysaccharide composed of β-1,4-linked glucopyranose residues.

These glucan chains are joined by inter-molecular hydrogen bonds and dispersive forces into partially crystalline microfibrils. The crystallinity and accessibility in native lignocellulose materials are thought to be a major factor contributing to “biomass recalcitrance”, which inhibit the accessibility by cellulolytic enzymes (Karimi and Taherzadeh, 2016). Meanwhile, the coalescence of microfibrils in the cell wall leads to larger macrofibrils with diameters up to 60 nm (Donaldson, 2007). This multi-scale organizations also contributes to the recalcitrance during enzymatic conversion. Thus, exploration for methods of efficiently deconstructing the cellulose-containing macromolecular complex, especially for the modification or disruption of crystalline cellulose, is key to a viable and desirable cellulosic biorefinery (Gomide et al., 2019).

The predominant allomorph in crystalline cellulose from plants is Iβ with two chains packed parallel in a monoclinic unit cell (Nishiyama et al., 2002). Due to its high density (1.63 g/cm^3, 1.60 for cellulose II, 1.54 for III_I, and 1.59 for III_{II}), cellulose Iβ is the form most difficult for enzymes to hydrolyze (Zhong et al., 2008). Therefore, it is important to establish pretreatment procedures to disrupt the compact structure of the Iβ allomorph and the tight association within microfibrils. Other cellulose allomorphs, including cellulose II, III and IV can be converted from cellulose I by different chemical treatments (Kim et al., 2013). Cellulose II is commonly created by alkaline treatment (also called mercerization) or the regeneration of dissolved cellulose. The formation of cellulose II from cellulose I is irreversible. We recently reported the effect of alkaline concentration on the allomorphic transformation from cellulose I to cellulose II (Ling et al., 2017). That work suggested that mercerization of moso bamboo began to take place by treatment with 8 wt% NaOH, while the complete allomorphic transformation occurred with 14 wt% NaOH. With antiparallel packing of its glucan chains, cellulose II crystals have a slightly enlarged spacing between adjacent cellulose sheets, reduced crystallite sizes, and typically decreased crystallinity (Horikawa et al., 2013; Nam et al., 2016). The supramolecular transformation and decrystallization from the NaOH treatment have improved the enzymatic digestibility of cellulose with an approximate 3-4-fold increase, widely expanding its application in biomass processing. Cellulose III_I can be prepared by soaking cellulose I in anhydrous liquid ammonia or in organic amines (Wada et al., 2004) and subsequent removal of the ammonia and amine. Cellulose III_I has a synergistically enhanced cellulase susceptibility because of a different hydrogen bond network and the greater distance between hydrophobic crystal planes (Chundawat et al., 2020, 2011; Igarashi et al., 2007). An 80% increase of glucose yield was achieved for ammonia induced cellulose III_I, though the increase was not as great as for cellulose II. It is likely attributable to the different crystallite sizes and lattice plane spacings for hydrophobic stacking surfaces between the two allomorphs (Sousa et al., 2019). In addition, the morphologically thinner fibrils caused a relatively lower enzymatic conversion efficiency than experienced for swollen and coarse cellulose II fibers (Jin et al., 2017; Ling et al., 2018). Real-time hydrolysis results indicated that cellulase slide unidirectionally along the cellulose III_I crystalline chains and halted collectively, causing traffic jams on the surface of the substrate (Igarashi et al., 2011).

To achieve an ideal enzymatic conversion yield of fermentable sugar from lignocellulosic biomass, allomorphic transformation is widely applied in conjunction with other treatments (Li et al., 2019; Wu et al., 2020; Yuan et al., 2018). Steam-assisted alkaline pretreatment, together with allomorphic transformation to cellulose II, facilitates the decrystallization of corn stalks, achieving a high glucose yield at a rather low enzyme loading (Liu et al., 2020). Stepwise pretreatments by aqueous ammonia and ethylenediamine (EDA) indicated that further conversion to cellulose III_I and amorphous cellulose took place at the EDA pretreatment stage, while aqueous ammonia was more responsible for swelling the fibrils and increasing the surface area (Zhu et al., 2018). EDA also enhanced the ionic liquid treatment of cellulose, which contributed to a mixture of cellulose II/III_I with extremely low crystallinity (Xu et al., 2020). The reported stepwise or co-pretreatments showed satisfactory cellulose deconstruction by efficient decrystallization and changing the allomorph from recalcitrant cellulose I. However, the allomorphic conversions were commonly performed with just one of the treatment stages. Rarely studied is the enhancement of pretreatment by successive allomorphic transformation, which could improve the efficiency of subsequent enzymatic hydrolysis.

In the present work, moso bamboo holocellulose and microcrystalline cellulose were stepwise pretreated first by NaOH or EDA and then with the other agents to unveil their effects on the efficiency of bioconversion. Cellulose III_{II} arises from NaOH treatment followed by EDA, and cellulose II results from treating first with EDA and then NaOH. The original as well as the single- and double-treated samples were then subjected to cellulase enzymatic hydrolysis. Thus, the effects of both allomorphic conversions on enzymatic digestibility of cellulose were systematically studied. The effects of these pretreatments on the multi-scale structures of cellulose and subsequent enzymatic degradation were characterized by chemical, microscopic, FTIR, Raman, X-ray diffraction and NMR analyses. These detailed studies involving various allomorphic transformations may provide better understanding of biomass recalcitrance from the point of view of cellulose supramolecular structure, which will guide the development of pretreatment protocols with lower enzyme and energy consumption.

2. Materials and methods

2.1 Materials

Moso bamboo (*Phyllostachy edulis*) was harvested from the Forestry Center in Sichuan Province, China. After milling with a Wiley mill to pass through an 80-mesh screen, the bamboo powder was treated by toluene/ethanol (2:1, v/v) Soxhlet extraction for 6 h to remove the extractives, followed by oven drying at 60 °C overnight. To remove the effects of lignin on the cellulose structural analyses, the extracted samples were treated by 30 wt% $NaClO_2$ at 75 °C for 4 h, at the solid/ liquid ratio of 1:15. Acetic acid (HAc) (2 wt%) was added each hour to keep the pH lower than 4.0. Microcrystalline cellulose (Avicel®, PH-101) was purchased from Sigma-Aldrich (Shanghai, China) as a model of the crystalline cellulose Iβ. The Raw moso bamboo, the delignified holocellulose from bamboo, and microcrystalline cellulose were named as MB, HC and MC respectively.

2.2 Stepwise pretreatments

The two-step allomorphic transformations of HC and MC were conducted according to the previous studies (Cheng et al., 2011; Horikawa et al., 2013). Cellulose II was obtained by soaking HC and MC in 14 wt% NaOH at 45 °C for 1 h, followed by filtration with deionized water, and oven drying at 60 °C overnight. The resulting alkali-treated samples were designated as HA and MA. Afterwards, HA and MA were treated with 75 % (v/v) EDA aqueous solution at room temperature for 24 h (Roche and Chanzy, 1981). After careful washing with ethanol and acetone, the cellulose III_{II} type HC and MC were respectively denoted as HAE and MAE. Similarly, with reversing the order of the alkaline and EDA stepwise treatments, cellulose III type samples HE/ME and alkali mercerized cellulose III samples HEA and MEA were obtained. All the samples were oven dried to remove the sample moisture to avoid effects on the subsequent enzymatic hydrolysis (Kobayashi et al., 2012). The treatment process and notation of the samples in this work are exhibited in Scheme. 1.

2.3 Characterization

Chemical compositions of the samples were determined by the National Renewable Energy Laboratory (NREL) protocol (Sluiter et al., 2012). Raman spectra were measured on a confocal laser micro-Raman spectrometer (Thermo Fischer DXR, USA) equipped with a diode laser of excitation of 532 nm (laser serial number: AJC1200566). The laser was focused onto the sample with an Olympus ×50 long distance objective. FTIR spectra of the samples were obtained by using the FTIR spectrometer (Thermo Nicolet™ 6700; Thermo Fisher Scientific, USA) at a resolution of 2 cm^{-1} and wavelengths from 4000 to 500 cm^{-1}. The spectrometer was equipped with an Attenuated Total Reflectance accessory (ATR-IR) and the ATR-IR spectra were baseline corrected by the software OMNIC 8.2 version.

^{13}C solid-state CP-MAS NMR spectra were acquired using a Bruker Advance III 400MHz; 9.4 Tesla) spectrometer with a 4 mm MAS HCN probe. The CP contact time was 1 ms and the magic-angle spinning frequency was 10 kHz.

Morphologies of the cellulose powders were observed by a JEOL JSM-7600F field emission scanning electron microscope (FESEM). Samples were coated with carbon and accelerating voltage was 15 kV. Meanwhile, longitudinal sections (12 μm, Leica SM2010R microtome) of moso bamboo holocellulose were also pretreated and scanned by an atomic force microscope (AFM, Bruker Dimension Edge) for exploring the microfibril swelling. Images of these sections were interpreted with NanoScope Analysis (Bruker) and ImageJ software to determine height distributions and fibril sizes.

Crystal structures of the various allomorphs were analyzed with a Rigaku Ultima IV X-ray diffractometer with Ni-filtered Cu-Kα radiation (λ = 0.1542 nm), generated at 35 kV and 40 mA. Scans were 5–40° (2θ) with scanning speed of 2°/min. Blank sample holder was also scanned for further subtraction by the powder patterns of cellulose samples. The patterns were analyzed using the pseudo-Voigt peak shape with Maud Rietveld software (Version 2.7) (Lutterotti et al., 2007). The crystallinity index (CrI) was calculated by Eq. (1), where A_{cryst} is the area below the calculated crystalline cellulose pattern and A_{amorph} is the area below the calculated amorphous curve.

$$\mathrm{CrI} = \frac{A_{crystal}}{A_{crystal}+A_{amorph}} \times 100\% \qquad (1)$$

The Rietveld analyses were based on the assumed presence of a single crystalline phase and an amorphous phase. The crystalline phase was chosen by the visual agreement of the observed pattern and the idealized patterns (French, 2014) and the expected allomorph, given the chemical treatments. The amorphous phase was modeled based on a small-crystal version of the cellulose II structure (Langan et al., 2001). The necessary crystal information files were taken from the supplementary materials in French (2014). Rietveld refinement variables included a second-order polynomial background, scale factor, *a*-, *b*-, and *γ* lattice constants, March-Dollase compensation for preferred (001) orientation and general (hkl) variation, isotropic crystallite size, and phase percentage.

The d-spacings were calculated from the refined unit cell dimensions via Bragg equation (Klug and Alexander, 1974):

$$n\lambda = 2d_{hkl}\sin\theta \quad (2)$$

where n is an integer; λ is the wave length of the X-rays (here λ = 0.1542 nm), θ is the scattering angle; and d is the distance between the atomic layers.

Crystallite sizes perpendicular to each lattice plane (L_{hkl}) of cellulose allomorphs were calculated by the Scherrer Equation (Eq. 3) (Holzwarth and Gibson, 2011):

$$L_{hkl} = \frac{0.9\lambda}{B_{hkl}\cos\theta} \quad (3)$$

Where λ is the X-ray wavelength, B_{hkl} is the angular FWHM (full width at half maximum) in radians of the calculated crystalline peaks, and θ is the scattering angle.

2.4 Enzymatic hydrolysis

Samples were hydrolyzed by commercial cellulase (SAE0020, Sigma-Aldrich) with the activity of 20 FPU/g of filter paper. Solid powder (0.5 g) was added in 50 mM citrate buffer (pH= 4.8) with a substrate loading of 5% (w/v). The reactions were run at

48 ℃ in a rotary shaker (150 rpm) for a total of 72 h. At times of 2 h, 12 h, 24 h, 36 h, 48 h, and 60 h, 0.1 mL hydrolysate aliquots were taken from the flask and centrifuged at 10000 rpm for 10 min to remove the solids. The concentration of the yielded glucose was determined by an Agilent 1200 high-performance liquid chromatograph (HPLC) (Lai et al., 2018). The glucose yield from enzymatic conversion was calculated using Eq. 4. All assays were performed in triplicate.

$$\text{Glucose yield } (\%) = \frac{Glucose\ in\ hydrolyzate\ (g) \times 0.9}{Initial\ glucan\ in\ substrate\ (g)} \times 100\% \qquad (4)$$

Where 0.9 is the correction for C-6 sugars for concentration calculation.

3. Results and discussion

3.1 Chemical composition

The chemical compositions of moso bamboo and the microcrystalline cellulose samples are presented in Table 1. Raw bamboo was dominated by cellulose (45.3%), followed by lignin (27.0%) and xylan type hemicelluloses (17.0%). Delignification diminished the lignin content to 10.3% for the HC sample. The alkaline and EDA pretreatments partly removed hemicelluloses and lignin as previously reported (Bali et al., 2015; Qin et al., 2015) , which retained most of the cellulose in the HA and HE materials. The second step of the pretreatment could not further reduce the xylan or lignin contents of the samples initially treated with NaOH but did reduce the xylan content of the samples first treated with EDA. We note that the hemicellulose content of the bamboo samples was sharply reduced in both HA and HEA samples. However, more hemicellulose was removed in the alkaline pretreatment than in the EDA pretreatment. The amount of lignin removed from HC by either NaOH or EDA was comparable. A small amount of xylan was detected in the MC samples, mainly due to the low-molecular-weight xylan retained during MC production (Yavorov et al., 2020). For MC-based samples, cellulose accounted for 85%-90%, when immersed in alkaline and EDA solutions.

3.2 Morphology

The morphologies of the stepwise treated MB and MC were observed by FESEM and AFM. As illustrated in FESEM images (Fig. S1), untreated MB has an intact and dense structure with cellulose fibers embedded in the lignin and hemicellulose matrix. After delignification, the long fibers were more visible for HC. Alkaline pretreatment smoothened the surface and loosened the condensed fibers while the EDA treatment resulted in rougher surfaces for HE and ME. Also, the swollen HA and MA fibers would return to a thinner and more condensed state after the second-step EDA treatment (HAE and MAE). HEA and MEA exposed the most visible macro- and microfibrils, indicating the importance of following the alkaline treatment with a second step of EDA treatment to further the disaggregation of the cellulose fibrils.

AFM images of HC longitudinal sections together with the size analyses on the microfibrils are displayed in Fig. 1. Height images from AFM were used to calculate the diameters of cellulose nanoparticles (Bian et al., 2020), except for the MB sections that had a high content of lignin covering the surface of cellulose fibrils (Fig. S2). After delignification, HC showed visible fibrillar structure, with tiny particles and cracks mainly due to the unremoved lignin. The average diameter of HC fibrils is 9.0 nm, slightly higher than the AFM-reported value for cellulose fibrils (Torlopov et al., 2018), which is attributable to the hemicellulose associated with cellulose by hydrogen bonding. Alkaline pretreatment not only removed the hemicellulose, but also twisted and swelled the cellulose microfibrils, resulting in a larger dimension of 11.3 nm (Fig. 1b). The second-step treatment of EDA led to an even larger average diameter (16.4 nm) for HAE microfibrils. However, for the one-step EDA pretreatment, the HE sample presented a sharp height distribution and fewer pores, with the average fibril size of 6.3 nm. A denser microfibril network has been reported for EDA-treated cellulose materials, likely caused by the conformational transitions of the primary alcohol hydroxyl group on C6 position (Liu et al., 2019; Sawada, Kimura, Nishiyama, Langan, & Wada, 2013). The second-step treatment with NaOH contributed to mild swelling of microfibrils and broader size distributions. More pores and higher surface area are observed from the AFM images of HEA (Fig. 1e), which might be beneficial for enzymatic permeability and biomass digestibility.

3.3 Spectroscopic characterizations

ATR-IR and Raman spectroscopy provided more information for chemical structural changes during the stepwise pretreatments (Fig. S3). The ATR-IR spectrum of MB shows typical peaks at 1600 cm^{-1} and 1740 cm^{-1} assigned to aromatic C-H stretching and the carbonyl groups in lignin. Those peaks are greatly reduced or even missing for other samples, proving the successful delignification for HC. Similar changes of the peak location at 1600 cm^{-1} were also detected in Raman spectra, further supporting the above results (Fig. S3c). Alkaline pretreatment significantly removed the xylan-type polysaccharides as indicated by the weakened peak intensity of carbohydrate carboxylic vibrations at 1245 cm^{-1}. The slight peak shift from 2900 cm^{-1} to 2892 cm^{-1} for HA and MA are due to the changes in the C-C stretching vibrations, which resulted from C6 groups rotating from *tg* conformation of cellulose I to the *gt* conformation of cellulose II or III. A sharp peak at 3481 cm^{-1} was visible for EDA treated cellulose, due to the strong intermolecular, bifurcated O3-H···O5’, O3-H···O6’ hydrogen bonding of cellulose III (Ford et al., 2005). Interestingly, the peak remained in the spectra of HEA and MEA samples, likely due to similar O6 orientations resembling that in cellulose III. The peak at 1372 cm^{-1} is generally considered to be characteristic for the crystalline part of cellulose (Carrillo et al., 2018). Besides, there is a significant increase of the band at 1462 cm^{-1} after both treatments, which contained the contributions of cellulose II/III as well as amorphous cellulose. It can be seen that the alkaline and EDA pretreatments both caused the decrease of the peak intensity in this area in spite of treatment order and the feedstock (Barnette et al., 2012; Fischer et al., 2005). It was seen that there appeared overlaps between the bands at 1481 cm^{-1} and 1462 cm^{-1}, probably due to residual hemicelluloses. The lower proportion of crystalline material may facilitate the subsequent hydrolysis.

The carbohydrate regions are presented in solid-state CP-MAS ^{13}C NMR spectra (Fig. 2). The HC and MC samples mainly have broad peaks at around 65.0 ppm that correspond to C6 groups with *tg* conformation in cellulose I (Agarwal et al., 2021; Horii et al., 1983; Li et al., 2017). The signals of *gt* conformations (and likely with some *gg* conformers) in the disordered domains or cellulose surface are expected at

62-63 ppm, but they exist as shoulder signals and remained unresolvable with the current spectral resolution limit. Spectra of the mercerized MA sample showed C6 signals toward 62 ppm and broader shoulder peaks at 106-107 ppm (instead of 105 ppm) for the C1 region, indicating the formation of cellulose II (Idström et al., 2016; S Nomura et al., 2020). A similar change in the C6 region was observed in the HA sample. These observations are consistent with the ATR-IR results described above.

The signals at 80-92 ppm are characteristic for C4 resonances in the interior and on the surface of the crystallites. The 80-85 ppm region mainly originates from amorphous cellulose on the surface and the 85-92 ppm region is due to the inaccessible crystalline cores (Foston, 2014; Maunu, Liitiä, Kauliomäki, Hortling, & Sundquist, 2000). For EDA-treated samples (HE and ME), it was observed that a significant shift of the dominant peak (C2, C3 and C5) appeared from 76 ppm to 72 ppm, indicative of the cellulose III allomorph (Chanzy et al., 1987). Deconvolution was conducted on 1D ^{13}C CP spectra with the DMfit software using a Gaussian model on a 50-120 ppm chemical shift window (Massiot et al., 2002). The simulated spectra (red) were overlaid with experimentally measured spectra (blue) (Fig. S4). The bottom panels show the deconvoluted peaks. This was achieved by directly loading the CP spectrum in the DMfit software, with a baseline correction applied. Six major peaks and three minor peaks were used for the fit convergence, with the assignment consistent with literature-reported cellulose chemical shifts mentioned above (Agarwal et al., 2021; Horii et al., 1983; Idström et al., 2016; Satoshi Nomura et al., 2020). Hemicellulose peaks are relatively minor. The computation and fit results gave the amplitude, widths, and peak area of different peaks.

The CrI of the pretreated celluloses can then be estimated by comparing the peak area of different spectral regions (Eq. 5):

$$\mathrm{CrI} = \frac{A_{85-92\ ppm}}{A_{80-85\ ppm}+A_{85-92\ ppm}} \times 100\% \tag{5}$$

Where the peak area of the 85-92 ppm region ($A_{85\text{-}92\ \mathrm{ppm}}$) corresponds to the signals of crystalline cellulose C4, with contributions from all cellulose polymorphs present in a sample, while the $A_{80\text{-}85\ \mathrm{ppm}}$ corresponds to the peak area of the 80-85 ppm region, which is primarily attributable to the interior cellulose C4.

This method carries a considerable error margin because of the limited resolution of 1D NMR spectra. Although matrix polysaccharides and lignin linkages have relatively low abundance in these samples, their signals overlap with the cellulose peaks, especially for the surface cellulose signals. Therefore, the crystallinity index reported for a sample rich in hemicellulose should be slightly lower than its actual value. Advanced solid-state NMR methods, such as relaxation-based spectral editing, selective excitation techniques, or natural isotropic-abundance methods, could partially alleviate this issue and provide a better estimate of cellulose crystallinity (Addison et al., 2020; Kang et al., 2019; Zhao et al., 2021).

3.4 Crystal structure analyses

XRD patterns directly indicate the particular allomorph and crystallite size in a sample (Fig. 3). For the HC and MC samples, typical peaks corresponding to (1-10), (110), and (200) lattice planes of cellulose Iβ were found at 2θ=14.8°, 16.8° and 22.5°. The (1-10), (110), and (020) lattice planes of cellulose II at 2θ=12.0°, 20.0° and 22.0°

are visible for the mercerized HA and MA samples (French, 2014; Nam et al., 2016). However, the one-step treatment seemed to achieve incomplete allomorphic transformation (especially for HA and HE) as the remained bands at around 2θ=16.8°, although the methods used here are commonly repeated. It may be ascribed to the high amount of hemicelluloses in HC samples, affecting the allomorphic transformation. Thus, the components of cellulose Iβ were firstly attempted to be included quantitatively in the following CrI calculations for these samples.

HAE and MAE showed cellulose III_{II} patterns with peaks at 2θ=12.1° and 2θ=21.0°, respectively ascribed to the hydrophilic (010) lattice planes and hydrophobic (1-10) lattice planes. HAE and MAE showed patterns similar to those of HE and ME, except for obviously larger peak widths, revealing (by applying Eq. 3) the smaller crystallite sizes after the second-step EDA treatment. The second-step of alkaline treatments caused the allomorphic transformations from cellulose III_I to cellulose II structure (HEA and MEA), which had patterns similar to cellulose II. Meanwhile, the broad peaks also proved the smaller crystallite sizes after the stepwise pretreatments.

The crystal structural determination (crystallite sizes and d-spacings perpendicular to crystal lattice planes) were responsible for analyzing the supramolecular variations and the properties of cellulose microfibrils. Specifically, hydrophobic planes are the sites of enzymatic adsorption and degradation of the crystals, which vary among the cellulose allomorphs (Lehtiö et al., 2003). Cellulose Iβ has hydrophobic (200) planes, while cellulose II and cellulose III_I basically have (020) and (1-10) crystal surface for adsorption by cellulase enzymes (Ling et al., 2018; Serizawa et al., 2013). HAE and

MAE samples have the cellulose III_{II} crystal structure with anti-parallel cellulose chains, which expose the hydrophobic (1-10) plane ($2\theta=21.0°$ in XRD patterns) (Wada et al., 2009). Meanwhile, HEA and MEA cellulose II are believed to have a similar hydrophobic (020) plane at around $2\theta=22.0°$. In this work, we considered the major cellulose allomorph (cellulose II for HA/MA and cellulose III_{I} for HE/ME) of each sample for discussing the crystallite sizes and d-spacings perpendicular to hydrophobic planes (Fig. 4). MC generally has larger crystallite sizes than bamboo cellulose. The increase of crystallite sizes and d-spacings from those in HC is more significant for HEA (0.4 nm) than HE, which would be greatly beneficial for the subsequent enzymatic hydrolysis. MAE and HAE (cellulose III_{II}) have slightly larger distances (both were 0.43 nm) between hydrophobic surfaces than initial cellulose Iβ crystals (0.405 nm and 0.398 nm for HC and MC, respectively). Comparatively, HE and ME had limited changes in crystallite sizes and d-spacings, which agreed with the tighter and thinner microfibril aggregations observed by AFM. The EDA pretreatment would therefore be expected to result in less efficient enzymatic conversion than the alkaline pretreatment.

The CrI values of the HC- and MC-based allomorphs are also key factors affecting enzymatic digestibility. CrI values were calculated based on both XRD and NMR data (Fig. 5). The selected equations and calculated values of CrI are recorded above (Ling et al., 2019). HC sample had a high CrI of 80% even though it was composed of 32% hemicelluloses. It may be due to some xylan chains located on the surface of the crystallites, which increased the calculated CrI (Xiang et al., 2020). These XRD CrI results showed that alkaline pretreatment caused a 20 % decrease of CrI for HA, while the decrease was not that notable for MA. More cellulose Iβ remained for MA, indicating a partial allomorphic conversion to cellulose II. Cellulose III samples based on the one-step EDA pretreatment were also less crystalline than the initial cellulose I samples (67% for HE and 57% for ME), although the treatment also remained little amount of cellulose Iβ. The stepwise treatments caused more significant decreases in the CrI values, especially for HEA and MEA, with rather low CrI values of 55% and 58%. Comparatively, the trend of CrI of each sample determined by XRD and NMR methods are similar (Fig. 5c and d). It is in accordance with previously reported crystallinity estimation by these measurements (Kim et al., 2013). It is estimated that, the sequential treatments are also responsible for the enlarged crystallites in addition to the lowered CrI. The EDA treatment on the first step changed the conformation of crystals, thus enhancing the rearrangements of cellulose chains during second-step alkaline mercerization. However, the exchanged order would inhibit the enhancement, which may be influenced by the condensing EDA-treated microfibrils by SEM. It also explained the recrystallization that induced slightly higher CrI of MAE than the MA from first-step alkaline pretreatment.

3.5 Enzymatic hydrolysis performance

The yields of fermentable glucose from these different allomorph/source cellulose samples are shown in Fig. 6. The delignification and a series of pretreatments greatly improved the cellulase enzymatic digestibility of cellulose (Fig. 6a), due to the gradually removed lignin and hemicelluloses. The one-step EDA pretreatment contributed to the significantly improved conversion values of 70.2% for HE and 69.8

for ME, which are, however, lower than the yield of HA (85.1%) and MA (86.9%). The phenomenon indicated the optimal hydrolysis performance by swelling and expanding cellulose microfibrils. After both treatments, HEA and MEA presented surprisingly high conversion yields of 89.5% and 91.7%, mainly due to the lower CrI as well as the cellulose II structure with expanded d-spacing for the hydrophobic (110) planes. There was limited enhancement on the enzymatic digestibility of HAE and MAE, possibly because of the less prominent decrystallization and the recrystallization behavior of cellulose III_{II} type MAE. The effects of xylan removal on the enzymatic conversion was exhibited in Fig. 6c. Five samples (HC, HA, HE, HAE and HEA) that can exactly reflect impacts of the embedded hemicelluloses were plot in this figure. It can be clearly seen that the high xylan removal yield during both treatments greatly improved the enzymatic hydrolysis yield. The relationships between d-spacings perpendicular to hydrophobic lattice plane and the enzymatic conversion is illustrated in Fig. 6d-f. By classifying and zoning the points with different allomorphs, it can be seen that the enlargement of hydrophobic d-spacing plays an important role in the enhancement of enzymatic conversion yield. Cellulase enzymes tend to adsorb the molecules on the hydrophobic lattice surfaces, contributing to better hydrolysis performance (Imai et al., 2020). When the crystallites swell to the state where the hydrophobic d-spacings are larger than 4.4 Å (MA, HEA and MEA), the glucose yield reached 90%. Generally, mercerized samples with cellulose II structure showed highest conversion yield, followed by EDA treated samples at the last step. Moreover, the trends were consistent at different time intervals, indicating the consistency of hydrolysis yields and hydrolysis kinetics.

Another key factor, CrI, is well-fitted with the glucose yield for the polymorphic cellulose (Fig. 6g-i). Optimal conversion rate and yield are obtained at low CrI region by comparing different hydrolysis time despite the type of the allomorphs, which is mainly due to the better enzymatic digestibility of amorphous cellulose. Taking the allomorphic transformation into consideration, samples with higher amount of cellulose II showed conversion yields higher than 80% especially for holocellulose samples, which agrees with above results on analyzing d-spacings.

3.6 Proposed structural modification by stepwise pretreatments

Satisfactory enzymatic hydrolysis performance was acquired for the stepwise pretreated samples together with the multistep allomorphic transformation. Multi-scale variations were observed to enhance the enzymatic digestibility. As presented in Fig. 7, two kinds of stepwise treatments lowered the density of the initial cellulose Iβ microfibrils, inducing the rearrangements of cellulose chains for cellulose III_{II} (HAE/MAE) and cellulose II (HEA/MEA). The two allomorphs both antiparallel cellulose chains induced by mercerization. The more evident decrystallization took place for cellulose II samples transformed from cellulose III_{II}, retaining a much thinner interior crystalline core and more accessible amorphous surfaces (Phyo et al., 2018). Meanwhile, the HEA and MEA elementary fibrils have enlarged spaces between crystalline cellulose chains, especially the direction perpendicular to hydrophobic planes. Therefore, the two-step allomorphic transformations caused loosened structure at multi-scale, by which the morphology and sizes of macro- and microfibrils were altered, in addition to the rearrangements of cellulose chain stacking. Deconstruction of cellulose multi structure, thus, may greatly improve the enzymatic hydrolysis performance for the stepwise pretreated polymorphic cellulose.

4. Conclusions

In conclusion, stepwise alkaline and EDA pretreatments were carried out with exchanged orders, resulting in the corresponding allomorphic transformations of moso bamboo and microcrystalline cellulose. The pretreatments improved the enzymatic conversion performance of bamboo and microcrystalline cellulose compared to one-step pretreatments, due to the loosened microfibril morphology, the lowered CrI and the rearranged crystal structure. Because of the enlarged hydrophobic d-spacings (~4.4 Å) and less- condensed microfibrils, highest enzymatic conversion yields of glucose were observed for HEA (89.5%) and MEA (91.7%). The proposed stepwise pretreatments emphasized the supramolecular structural variations of the renewable cellulose materials as well as the importance of treatment in the bioconversion processes.

E-supplementary data of this work can be found in online version of the paper.

Acknowledgements

The authors acknowledge the funding support from the National Natural Science Foundation for Youth (32001270) and Natural Science Foundation of Jiangsu Province for Youth (BK20200797). TW and AK were supported by the U.S. Department of Energy (grant no. DE-SC0021210). We also appreciate prof. Mengmeng Fan in Nanjing Forestry University for helping on NMR detection on the samples.

References

Addison, B., Stengel, D., Bharadwaj, V.S., Happs, R.M., Doeppke, C., Wang, T., Bomble, Y.J., Holland, G.P., Harman-Ware, A.E., 2020. Selective One-Dimensional 13C–13C Spin-Diffusion Solid-State Nuclear Magnetic Resonance Methods to Probe Spatial Arrangements in Biopolymers Including Plant Cell Walls, Peptides, and Spider Silk. J. Phys. Chem. B 124, 9870–9883. https://doi.org/10.1021/acs.jpcb.0c07759

Agarwal, U.P., Reiner, R.S., Ralph, S.A., Catchmark, J., Chi, K., Foster, E.J., Hunt, C.G., Baez, C., Ibach, R.E., Hirth, K.C., 2021. Characterization of the supramolecular structures of cellulose nanocrystals of different origins. Cellulose 28, 1369–1385. https://doi.org/10.1007/s10570-020-03590-z

Bali, G., Meng, X., Deneff, J.I., Sun, Q., Ragauskas, A.J., 2015. The effect of alkaline pretreatment methods on cellulose structure and accessibility. ChemSusChem 8, 275–279. https://doi.org/10.1002/cssc.201402752

Barnette, A.L., Lee, C., Bradley, L.C., Schreiner, E.P., Park, Y.B., Shin, H., Cosgrove, D.J., Park, S., Kim, S.H., 2012. Quantification of crystalline cellulose in lignocellulosic biomass using sum frequency generation (SFG) vibration spectroscopy and comparison with other analytical methods. Carbohydr. Polym. 89, 802–809. https://doi.org/https://doi.org/10.1016/j.carbpol.2012.04.014

Bian, H., Dong, M., Chen, L., Zhou, X., Wang, R., Jiao, L., Ji, X., Dai, H., 2020. On-demand regulation of lignocellulosic nanofibrils based on rapid fractionation using acid hydrotrope: Kinetic study and characterization. ACS Sustain. Chem.

Eng. 8, 9569–9577.

Carrillo, I., Mendonça, R.T., Ago, M., Rojas, O.J., 2018. Comparative study of cellulosic components isolated from different Eucalyptus species. Cellulose 25, 1011–1029.

Chanzy, H., Henrissat, B., Vincendon, M., Tanner, S.F., Belton, P.S., 1987. Solid-state 13C-N.M.R. and electron microscopy study on the reversible cellulose I→cellulose IIII transformation in Valonia. Carbohydr. Res. 160, 1–11. https://doi.org/https://doi.org/10.1016/0008-6215(87)80299-9

Cheng, G., Varanasi, P., Li, C., Liu, H., Melnichenko, Y.B., Simmons, B.A., Kent, M.S., Singh, S., 2011. Transition of cellulose crystalline structure and surface morphology of biomass as a function of ionic liquid pretreatment and its relation to enzymatic hydrolysis. Biomacromolecules 12, 933–941. https://doi.org/10.1021/bm101240z

Chundawat, S.P.S., Bellesia, G., Uppugundla, N., Da Costa Sousa, L., Gao, D., Cheh, A.M., Agarwal, U.P., Bianchetti, C.M., Phillips, G.N., Langan, P., Balan, V., Gnanakaran, S., Dale, B.E., 2011. Restructuring the crystalline cellulose hydrogen bond network enhances its depolymerization rate. J. Am. Chem. Soc. 133, 11163–11174. https://doi.org/10.1021/ja2011115

Chundawat, S.P.S., Sousa, L.D.C., Roy, S., Yang, Z., Gupta, S., Pal, R., Zhao, C., Liu, S.H., Petridis, L., O'Neill, H., Pingali, S.V., 2020. Ammonia-salt solvent promotes cellulosic biomass deconstruction under ambient pretreatment conditions to enable rapid soluble sugar production at ultra-low enzyme loadings. Green Chem. 22, 204–218. https://doi.org/10.1039/c9gc03524a

Donaldson, L., 2007. Cellulose microfibril aggregates and their size variation with cell wall type. Wood Sci. Technol. 41, 443–460. https://doi.org/10.1007/s00226-006-0121-6

Fischer, S., Schenzel, K., Fischer, K., Diepenbrock, W., 2005. Applications of FT Raman Spectroscopy and Micro Spectroscopy Characterizing Cellulose and Cellulosic Biomaterials. Macromol. Symp. 223, 41–56. https://doi.org/https://doi.org/10.1002/masy.200550503

Ford, Z.M., Stevens, E.D., Johnson, G.P., French, A.D., 2005. Determining the crystal structure of cellulose IIII by modeling. Carbohydr. Res. 340, 827–833. https://doi.org/https://doi.org/10.1016/j.carres.2005.01.028

Foston, M., 2014. Advances in solid-state NMR of cellulose. Curr. Opin. Biotechnol. 27, 176–184. https://doi.org/10.1016/j.copbio.2014.02.002

French, A.D., 2014. Idealized powder diffraction patterns for cellulose polymorphs. Cellulose 21, 885–896. https://doi.org/10.1007/s10570-013-0030-4

Gomide, F.T.F., da Silva, A.S., da Silva Bon, E.P., Alves, T.L.M., 2019. Modification of microcrystalline cellulose structural properties by ball-milling and ionic liquid treatments and their correlation to enzymatic hydrolysis rate and yield. Cellulose 26, 7323–7335.

Holzwarth, U., Gibson, N., 2011. The Scherrer equation versus the’Debye-Scherrer equation’. Nat. Nanotechnol. 6, 534.

Horii, F., Hirai, A., Kitamaru, R., 1983. Solid-state 13C-NMR study of conformations of oligosaccharides and cellulose. Polym. Bull. 10, 357–361. https://doi.org/10.1007/BF00281948

Horikawa, Y., Konakahara, N., Imai, T., Kentaro, A., Kobayashi, Y., Sugiyama, J., 2013. The structural changes in crystalline cellulose and effects on enzymatic digestibility. Polym. Degrad. Stab. 98, 2351–2356. https://doi.org/10.1016/j.polymdegradstab.2013.08.004

Idström, A., Schantz, S., Sundberg, J., Chmelka, B.F., Gatenholm, P., Nordstierna, L., 2016. 13C NMR assignments of regenerated cellulose from solid-state 2D NMR spectroscopy. Carbohydr. Polym. 151, 480–487. https://doi.org/https://doi.org/10.1016/j.carbpol.2016.05.107

Igarashi, K., Koivula, A., Wada, M., Kimura, S., Okamoto, T., Ando, T., Samejima, M., 2011. Corrected 28 october 2011; see last page 6. 187.

Igarashi, K., Wada, M., Samejima, M., 2007. Activation of crystalline cellulose to cellulose IIII results in efficient hydrolysis by cellobiohydrolase. FEBS J. 274, 1785–1792. https://doi.org/10.1111/j.1742-4658.2007.05727.x

Imai, M., Horikawa, Y., Kiyoto, S., Imai, T., Sugiyama, J., 2020. Structural changes in sugarcane bagasse cellulose caused by enzymatic hydrolysis. J. Wood Sci. 66, 1–8.

Jin, E., Zhang, Y., Hu, F., Yang, F., Wu, S., Jin, Y., Song, J., 2017. To understand the superior hydrolytic activity after polymorphic conversion from cellulose I to II from the adsorption behaviors of enzymes. Cellulose. https://doi.org/10.1007/s10570-016-1183-8

Kang, X., Kirui, A., Widanage, M.C.D., Mentink-Vigier, F., Cosgrove, D.J., Wang, T., 2019. Lignin-polysaccharide interactions in plant secondary cell walls revealed by solid-state NMR. Nat. Commun. 10, 1–9.

Karimi, K., Taherzadeh, M.J., 2016. A critical review of analytical methods in pretreatment of lignocelluloses: Composition, imaging, and crystallinity. Bioresour. Technol. 200, 1008–1018. https://doi.org/10.1016/j.biortech.2015.11.022

Kim, S.H., Lee, C.M., Kafle, K., 2013. Characterization of crystalline cellulose in biomass: Basic principles, applications, and limitations of XRD, NMR, IR, Raman, and SFG. Korean J. Chem. Eng. 30, 2127–2141. https://doi.org/10.1007/s11814-013-0162-0

Klug, H.P., Alexander, L.E., 1974. X-ray diffraction procedures: for polycrystalline and amorphous materials. X-Ray Diffr. Proced. Polycryst. Amorph. Mater. 2nd Ed. by Harold P. Klug, Leroy E. Alexander, pp. 992. ISBN 0-471-49369-4. Wiley-VCH, May 1974. 992.

Kobayashi, K., Kimura, S., Kim, U.-J., Tokuyasu, K., Wada, M., 2012. Enzymatic hydrolysis of cellulose hydrates. Cellulose 19, 967–974. https://doi.org/10.1007/s10570-012-9696-2

Lai, C., Yang, B., He, J., Huang, C., Li, X., Song, X., Yong, Q., 2018. Enhanced enzymatic digestibility of mixed wood sawdust by lignin modification with naphthol derivatives during dilute acid pretreatment. Bioresour. Technol. 269, 18–24.

Langan, P., Nishiyama, Y., Chanzy, H., 2001. X-ray Structure of Mercerized Cellulose II at 1 ! Resolution X-ray Structure of Mercerized Cellulose II at 1 Å Resolution. Cellulose 2, 410–416. https://doi.org/10.1021/bm005612q

Lehtiö, J., Sugiyama, J., Gustavsson, M., Fransson, L., Linder, M., Teeri, T.T., 2003. The binding specificity and affinity determinants of family 1 and family 3 cellulose binding modules. Proc. Natl. Acad. Sci. 100, 484–489. https://doi.org/10.1073/pnas.212651999

Li, J., Shi, J., Medina, J.E., Zhou, J., Du, X., Wang, H., Yang, C., Liu, J., Yang, Z., Dinulescu, D.M., Xu, B., 2017. Selectively Inducing Cancer Cell Death by Intracellular Enzyme-Instructed Self-Assembly (EISA) of Dipeptide Derivatives. Adv. Healthc. Mater. 6, 1–9. https://doi.org/10.1002/adhm.201601400

Li, P., Zhang, Q., Zhang, Xun, Zhang, Xueming, Pan, X., Xu, F., 2019. Subcellular dissolution of xylan and lignin for enhancing enzymatic hydrolysis of microwave assisted deep eutectic solvent pretreated Pinus bungeana Zucc. Bioresour. Technol. 288, 121475.

Ling, Z., Chen, S., Zhang, X., Xu, F., 2017. Exploring crystalline-structural variations of cellulose during alkaline pretreatment for enhanced enzymatic hydrolysis. Bioresour. Technol. 224, 611–617. https://doi.org/10.1016/j.biortech.2016.10.064

Ling, Z., Wang, T., Makarem, M., Santiago Cintrón, M., Cheng, H.N., Kang, X., Bacher, M., Potthast, A., Rosenau, T., King, H., Delhom, C.D., Nam, S., Vincent Edwards, J., Kim, S.H., Xu, F., French, A.D., 2019. Effects of ball milling on the structure of cotton cellulose. Cellulose 26, 305–328. https://doi.org/10.1007/s10570-018-02230-x

Ling, Z., Zhang, X., Yang, G., Takabe, K., Xu, F., 2018. Nanocrystals of cellulose allomorphs have different adsorption of cellulase and subsequent degradation. Ind. Crops Prod. 112, 541–549.

Liu, C., Liu, M., Wang, P., Chang, J., Yin, Q., Zhu, Q., Lu, F., 2020. Effect of steam-assisted alkaline pretreatment plus enzymolysis on converting corn stalk into reducing sugar. Renew. Energy 159, 982–990. https://doi.org/https://doi.org/10.1016/j.renene.2020.06.084

Liu, Z., Wu, J., Xia, J., Dai, H., Cao, Y., Wang, Z., 2019. Characterization of lignocellulose aerogels fabricated using a LiCl/DMSO solution. Ind. Crops Prod. 131, 293–300. https://doi.org/https://doi.org/10.1016/j.indcrop.2019.01.057

Lutterotti, L., Bortolotti, M., Ischia, G., Lonardelli, I., Wenk, H.R., 2007. Rietveld texture analysis from diffraction images. Z. Krist. Suppl 26, 125–130.

Massiot, D., Fayon, F., Capron, M., King, I., Le Calvé, S., Alonso, B., Durand, J., Bujoli, B., Gan, Z., Hoatson, G., 2002. Modelling one-and two-dimensional solid-state NMR spectra. Magn. Reson. Chem. 40, 70–76.

Maunu, S., Liitiä, T., Kauliomäki, S., HORTLING, B.O., SUNDQUIST, J., 2000. 13C CPMAS NMR investigations of cellulose polymorphs in different pulps. Cellulose 7, 147–159. https://doi.org/10.1023/A:1009200609482

Mosier, N.S., Ladisch, C.M., Ladisch, M.R., 2002. Characterization of acid catalytic domains for cellulose hydrolysis and glucose degradation. Biotechnol. Bioeng.

79, 610–618.

Nam, S., French, A.D., Condon, B.D., Concha, M., 2016. Segal crystallinity index revisited by the simulation of X-ray diffraction patterns of cotton cellulose I?? and cellulose II. Carbohydr. Polym. 135, 1–9. https://doi.org/10.1016/j.carbpol.2015.08.035

Nishiyama, Y., Langan, P., Chanzy, H., 2002. Crystal structure and hydrogen-bonding system in cellulose Iβ from synchrotron X-ray and neutron fiber diffraction. J. Am. Chem. Soc. 124, 9074–9082.

Nomura, S, Kugo, Y., Erata, T., 2020. 13C NMR and XRD studies on the enhancement of cellulose II crystallinity with low concentration NaOH post-treatments. Cellulose.

Nomura, Satoshi, Kugo, Y., Erata, T., 2020. 13C NMR and XRD studies on the enhancement of cellulose II crystallinity with low concentration NaOH post-treatments. Cellulose 27, 3553–3563. https://doi.org/10.1007/s10570-020-03036-6

Phyo, P., Wang, T., Yang, Y., O’Neill, H., Hong, M., 2018. Direct determination of hydroxymethyl conformations of plant cell wall cellulose using 1H polarization transfer solid-state NMR. Biomacromolecules 19, 1485–1497.

Qin, L., Li, W.C., Zhu, J.Q., Liang, J.N., Li, B.Z., Yuan, Y.J., 2015. Ethylenediamine pretreatment changes cellulose allomorph and lignin structure of lignocellulose at ambient pressure. Biotechnol Biofuels 8, 174. https://doi.org/10.1186/s13068-015-0359-z

Roche, E., Chanzy, H., 1981. Electron microscopy study of the transformation of cellulose I into cellulose IIII in Valonia. Int. J. Biol. Macromol. 3, 201–206. https://doi.org/10.1016/0141-8130(81)90064-7

Sawada, D., Kimura, S., Nishiyama, Y., Langan, P., Wada, M., 2013. The crystal structure of mono-ethylenediamine β-chitin from synchrotron X-ray fiber diffraction. Carbohydr. Polym. 92, 1737–1742. https://doi.org/https://doi.org/10.1016/j.carbpol.2012.11.025

Serizawa, T., Sawada, T., Okura, H., Wada, M., 2013. Hydrolytic activities of crystalline cellulose nanofibers. Biomacromolecules 14, 613–617. https://doi.org/10.1021/bm4000822

Sluiter, A., Hames, B., Ruiz, R., Scarlata, C., Sluiter, J., Templeton, D., Nrel, D.C., 2012. Determination of Structural Carbohydrates and Lignin in Biomass Determination of Structural Carbohydrates and Lignin in Biomass 2011.

Sousa, L.D.C., Humpula, J., Balan, V., Dale, B.E., Chundawat, S.P.S., 2019. Impact of Ammonia Pretreatment Conditions on the Cellulose III Allomorph Ultrastructure and Its Enzymatic Digestibility. ACS Sustain. Chem. Eng. 7, 14411–14424. https://doi.org/10.1021/acssuschemeng.9b00606

Torlopov, M.A., Mikhaylov, V.I., Udoratina, E. V, Aleshina, L.A., Prusskii, A.I., Tsvetkov, N. V, Krivoshapkin, P. V, 2018. Cellulose nanocrystals with different length-to-diameter ratios extracted from various plants using novel system acetic acid/phosphotungstic acid/octanol-1. Cellulose 25, 1031–1046. https://doi.org/10.1007/s10570-017-1624-z

Wada, M., Chanzy, H., Nishiyama, Y., Langan, P., 2004. Cellulose III I crystal structure and hydrogen bonding by synchrotron X-ray and neutron fiber diffraction. Macromolecules 37, 8548–8555. https://doi.org/10.1021/ma0485585

Wada, M., Heux, L., Nishiyama, Y., Langan, P., 2009. X-ray Crystallographic, Scanning Microprobe X-ray Diffraction, and Cross-Polarized/Magic Angle Spinning 13C NMR Studies of the Structure of Cellulose IIIII. Biomacromolecules 10, 302–309. https://doi.org/10.1021/bm8010227

Wu, J., Chandra, R.P., Kim, K.H., Kim, C.S., Pu, Y., Ragauskas, A.J., Saddler, J.N., 2020. Enhancing enzyme-mediated hydrolysis of mechanical pulps by deacetylation and delignification. ACS Sustain. Chem. Eng. 8, 5847–5855.

Xiang, Z., Jin, X., Huang, C., Li, L., Wu, W., Qi, H., Nishiyama, Y., 2020. Water cast film formability of sugarcane bagasse xylans favored by side groups. Cellulose 27, 7307–7320. https://doi.org/10.1007/s10570-020-03291-7

Xu, L., Li, W.-C., Xin, J., Zhang, S.-J., Li, B.-Z., Yuan, Y.-J., 2020. Ethylenediamine Enhances Ionic Liquid Pretreatment Performance at High Solid Loading. ACS Sustain. Chem. Eng. https://doi.org/10.1021/acssuschemeng.0c03884

Yavorov, N., Valchev, I., Radeva, G., Todorova, D., 2020. Kinetic investigation of dilute acid hydrolysis of hardwood pulp for microcrystalline cellulose production. Carbohydr. Res. 488, 107910. https://doi.org/https://doi.org/10.1016/j.carres.2020.107910

Yuan, Z., Li, G., Hegg, E.L., 2018. Enhancement of sugar recovery and ethanol production from wheat straw through alkaline pre-extraction followed by steam pretreatment. Bioresour. Technol. 266, 194–202. https://doi.org/https://doi.org/10.1016/j.biortech.2018.06.065

Zhao, W., Kirui, A., Deligey, F., Mentink-Vigier, F., Zhou, Y., Zhang, B., Wang, T., 2021. Solid-state NMR of unlabeled plant cell walls: high-resolution structural analysis without isotopic enrichment. Biotechnol. Biofuels 14, 14. https://doi.org/10.1186/s13068-020-01858-x

Zhong, L., Matthews, J.F., Crowley, M.F., Rignall, T., Talón, C., Cleary, J.M., Walker, R.C., Chukkapalli, G., McCabe, C., Nimlos, M.R., 2008. Interactions of the complete cellobiohydrolase I from Trichodera reesei with microcrystalline cellulose Iβ. Cellulose 15, 261–273.

Zhu, J.Q., Li, W.C., Qin, L., Zhao, X., Chen, S., Liu, H., Liu, Z.H., Zhou, X., Li, X., Li, B.Z., Yuan, Y.J., 2018. Stepwise pretreatment of aqueous ammonia and ethylenediamine improve enzymatic hydrolysis of corn stover. Ind. Crops Prod. 124, 201–208. https://doi.org/10.1016/j.indcrop.2018.07.072

Table 1. Chemical compositions of moso bamboo and microcrystalline cellulose before and after various pretreatments.

	Glucan (%)	**Xylan (%)**	**Insoluble Lignin (%)[a]**	**Soluble Lignin (%)**	**Lignin (%)**	**Solid Recovery (%)**
MB	45.3 ± 0.8	17.0 ± 1.3	25.6 ± 1.3	1.4 ± 0.08	27.0 ± 2.1	-
HC	57.9 ± 0.7	22.0 ± 2.5	9.8 ± 1.2	0.5 ± 0.10	10.3 ± 1.3	76.6 ± 1.8
HA	84.3 ± 0.3	6.9 ± 0.4	1.1 ± 0.2	0.4 ± 0.10	1.5 ± 0.3	52.4 ± 1.3
HAE	81.7 ± 0.3	7.5 ± 0.5	1.1 ± 0.1	0.2 ± 0.05	1.3 ± 0.2	49.2 ± 0.9
HE	78.6 ± 1.2	11.7 ± 1.5	1.1 ± 0.2	0.8 ± 0.08	1.9 ± 0.3	50.7 ± 1.1
HEA	86.9 ± 0.3	6.4 ± 0.2	1.0 ± 0.1	0.8 ± 0.02	1.8 ± 0.2	42.4 ± 1.2
MC	85.2 ± 0.1	7.8 ± 0.6	-	-	-	-
MA	88.0 ± 0.1	6.5 ± 0.3	-	-	-	95.3 ± 1.4
MAE	84.7 ± 1.1	5.6 ± 0.2	-	-	-	96.1 ± 1.3
ME	85.3 ± 0.4	7.0 ± 0.5	-	-	-	94.9 ± 1.1
MEA	89.4 ± 0.9	5.7 ± 0.3	-	-	-	91.6 ± 1.0

[a] Lignin was not detected in microcrystalline cellulose samples.

Figure Captions:

Scheme. 1. The treatment process and acronym denotation for each sample.

Fig. 1. AFM images and height distribution for HC (a), HA (b), HAE (c), HE (d) and HEA (e). The best-fit Gaussian curve and the averaged fibril diameter are shown for each sample.

Fig. 2. ^{13}C solid-state CP-MAS NMR spectra of the HC and MC powders before and after the stepwise pretreatments. The type-assignments for the major peaks are labeled. Dashlines were used to guide the comparison between samples.

Fig. 3. XRD patterns of HC (a) and MC (b) samples with different allomorphic transformation treatments.

Fig. 4. The crystallite sizes (a) and d-spacings (b) perpendicular to hydrophobic crystal lattice planes of each sample. Blue columns represent holocellulose and red columns represent microcrystalline cellulose.

Fig. 5. CrI values of (a) polymorphic holocellulose cellulose and (b) microcrystalline cellulose samples calculated by XRD and their comparisons with CrI value obtained from NMR spectroscopy.

Fig. 6. Enzymatic conversion yields of glucose for polymorphic cellulose derived from (a) moso bamboo and (b) microcrystalline cellulose; The fitting results on the relationship between conversion yield and remaining xylan content (c), d-spacing perpendicular to hydrophobic planes (d, e, f) and crystallinity index (g, h, i) at time intervals of 24 h (d, g), 48 h (e, h) and 72 h (f, i).

Fig. 7. Proposed schematic models for the crystalline cellulose after the stepwise

alkaline-EDA (a) and EDA-alkaline (b) pretreatments.

Figures:

Scheme. 1

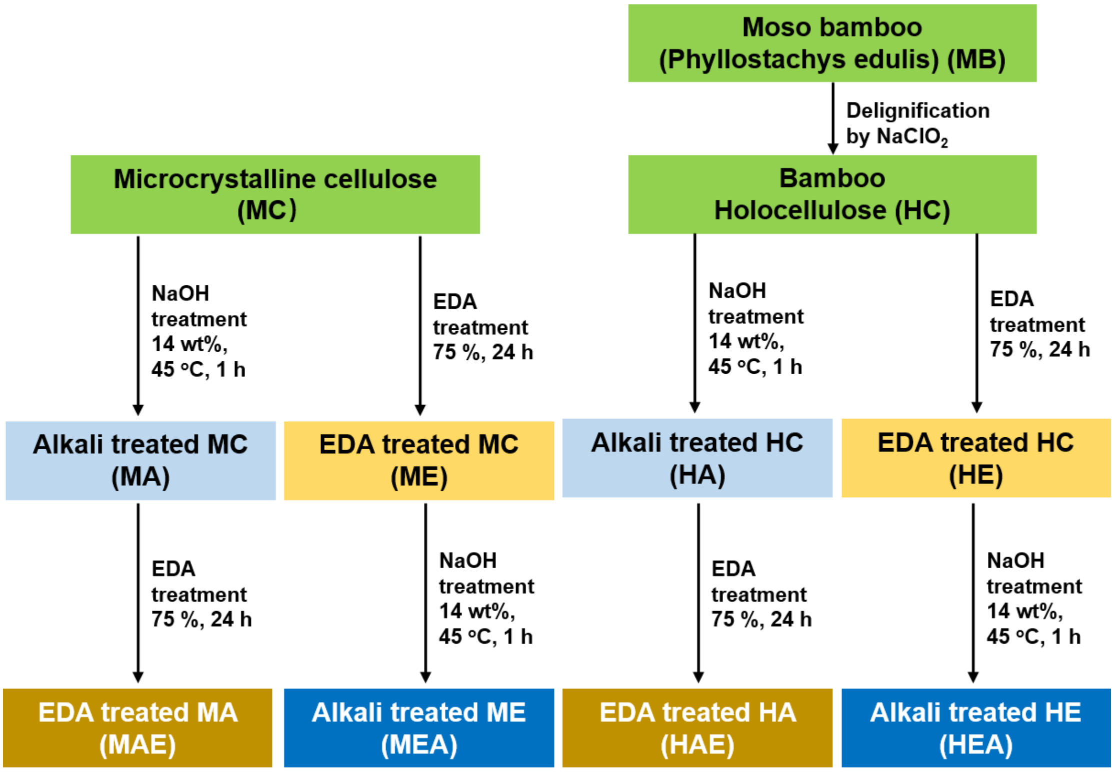

Fig. 1

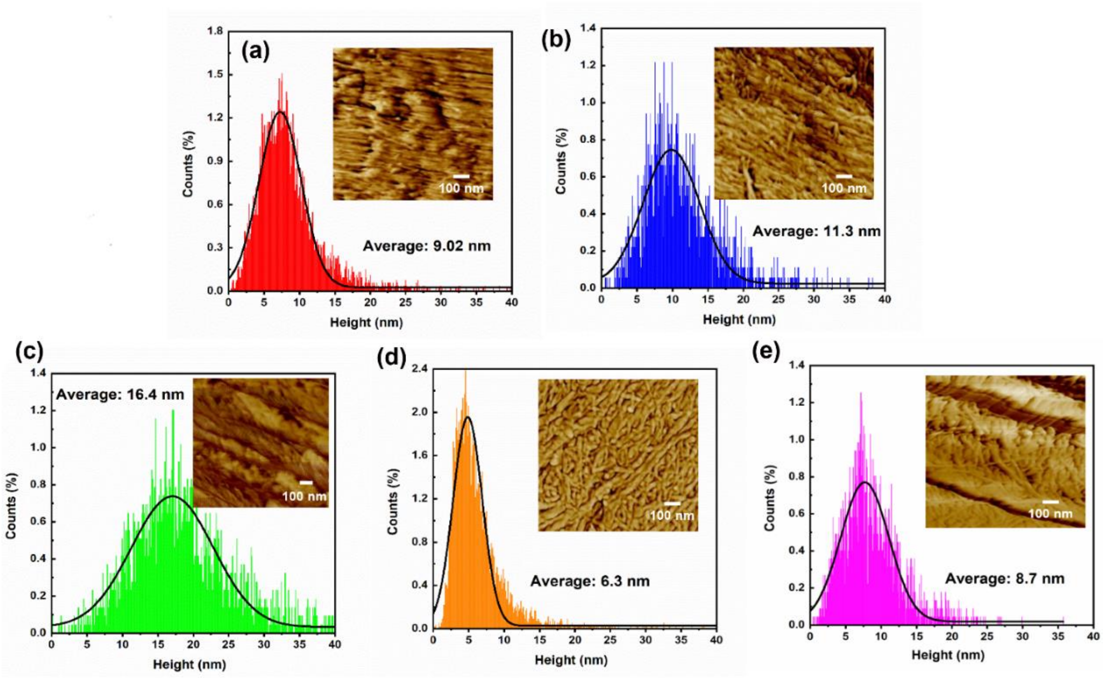
(a)
Average: 9.02 nm
(b)
Average: 11.3 nm
(c)
Average: 16.4 nm
(d)
Average: 6.3 nm
(e)
Average: 8.7 nm
100 nm
Counts (%)
Height (nm)

Fig. 2

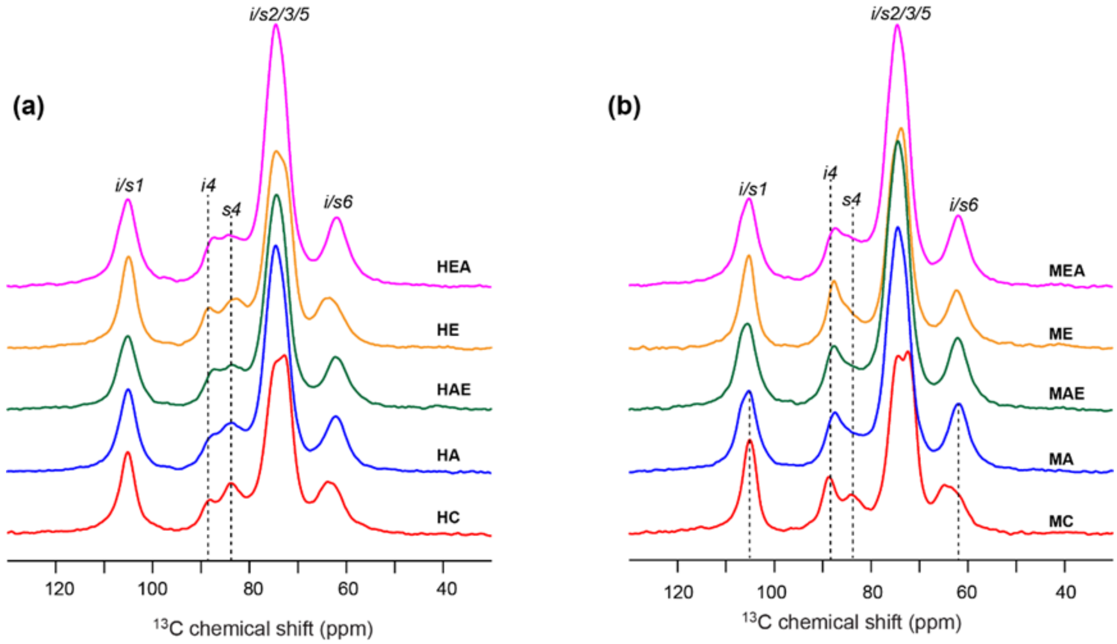
(a)
i/s2/3/5
i/s1
i4
s4
i/s6
HEA
HE
HAE
HA
HC
120
100
80
60
40
^{13}C chemical shift (ppm)
(b)
i/s2/3/5
i/s1
i4
s4
i/s6
MEA
ME
MAE
MA
MC
120
100
80
60
40
^{13}C chemical shift (ppm)

Fig. 3

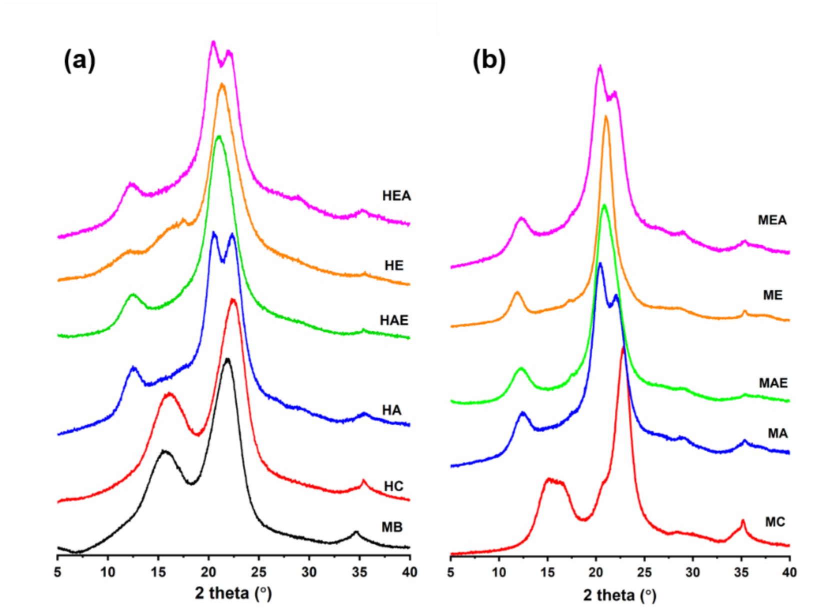
(a)
HEA
HE
HAE
HA
HC
MB
5 10 15 20 25 30 35 40
2 theta (°)
(b)
MEA
ME
MAE
MA
MC
5 10 15 20 25 30 35 40
2 theta (°)

Fig. 4

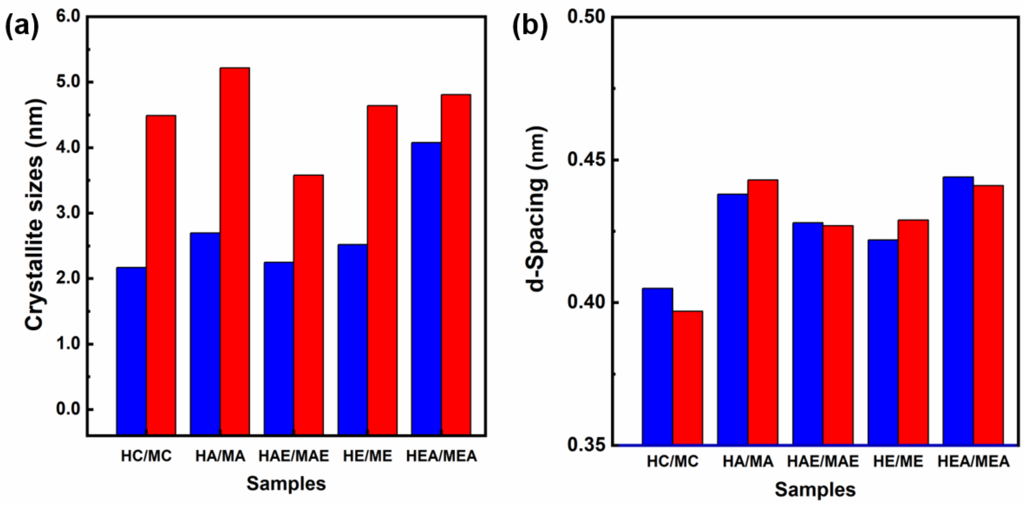
(a)
Crystallite sizes (nm)
6.0
5.0
4.0
3.0
2.0
1.0
0.0
HC/MC
HA/MA
HAE/MAE
HE/ME
HEA/MEA
Samples
(b)
d-Spacing (nm)
0.50
0.45
0.40
0.35
HC/MC
HA/MA
HAE/MAE
HE/ME
HEA/MEA
Samples

Fig. 5

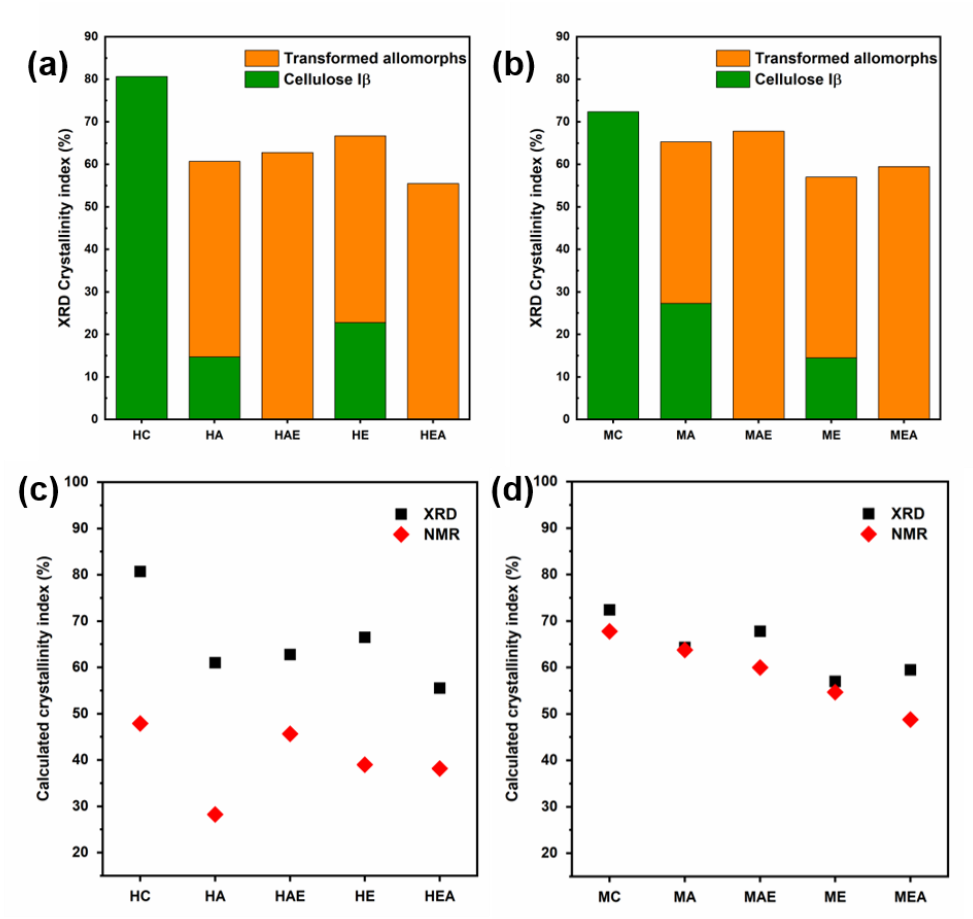
(a)
(b)
(c)
(d)
Transformed allomorphs
Cellulose Iβ
XRD Crystallinity index (%)
HC
HA
HAE
HE
HEA
MC
MA
MAE
ME
MEA
XRD
NMR
Calculated crystallinity index (%)

Fig. 6

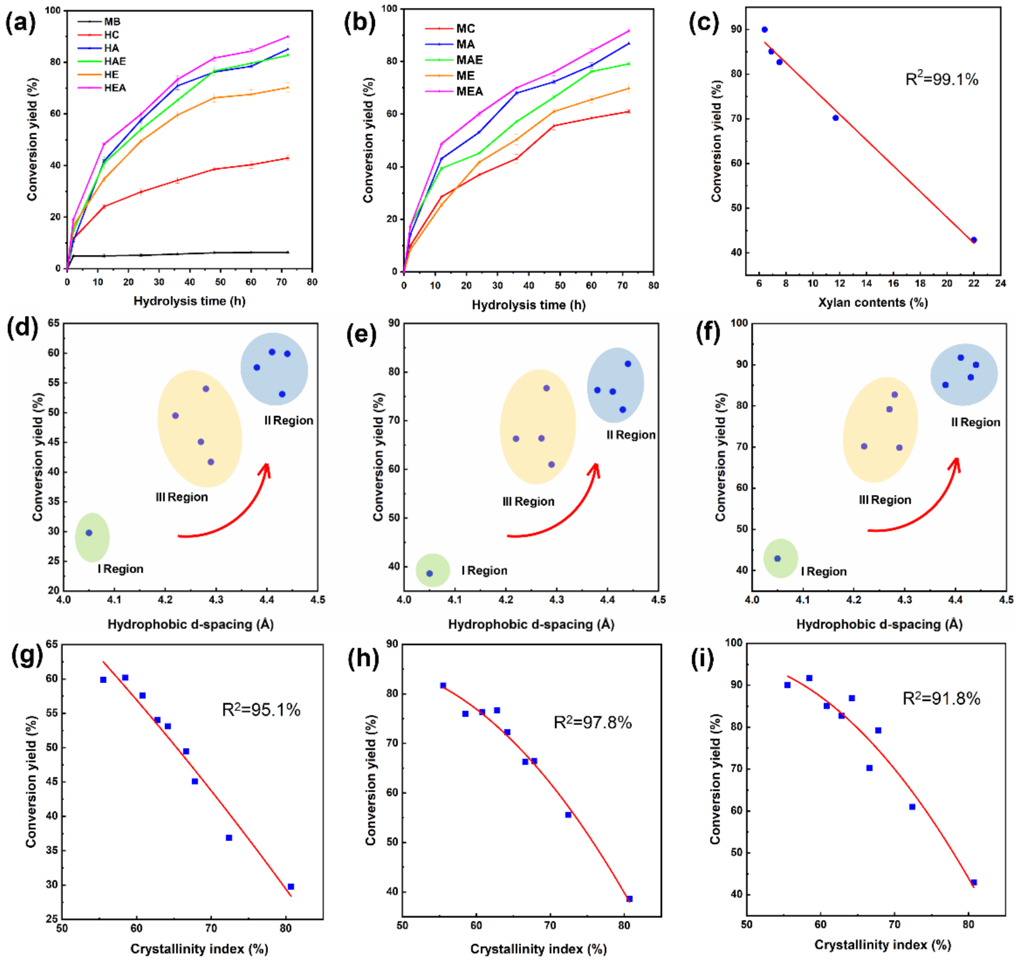

(a)
MB
HC
HA
HAE
HE
HEA
Conversion yield (%)
Hydrolysis time (h)
(b)
MC
MA
MAE
ME
MEA
Conversion yield (%)
Hydrolysis time (h)
(c)
R²=99.1%
Conversion yield (%)
Xylan contents (%)
(d)
II Region
III Region
I Region
Conversion yield (%)
Hydrophobic d-spacing (Å)
(e)
II Region
III Region
I Region
Conversion yield (%)
Hydrophobic d-spacing (Å)
(f)
II Region
III Region
I Region
Conversion yield (%)
Hydrophobic d-spacing (Å)
(g)
R²=95.1%
Conversion yield (%)
Crystallinity index (%)
(h)
R²=97.8%
Conversion yield (%)
Crystallinity index (%)
(i)
R²=91.8%
Conversion yield (%)
Crystallinity index (%)

Fig. 7

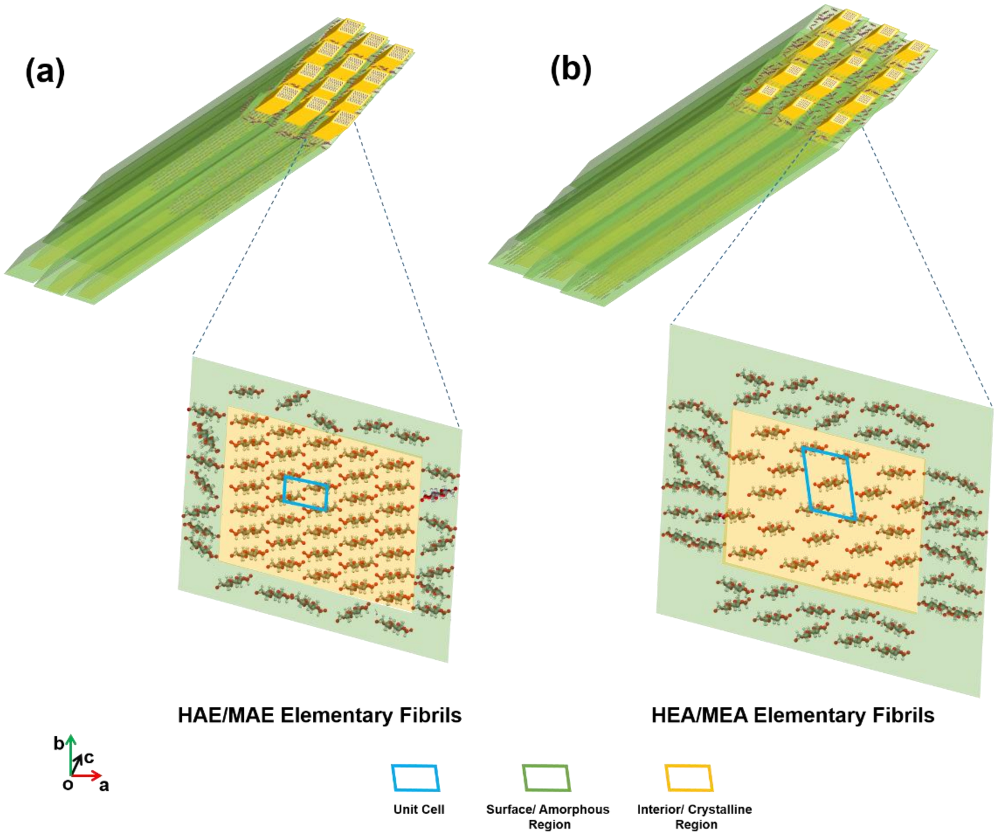
(a)
(b)
HAE/MAE Elementary Fibrils
HEA/MEA Elementary Fibrils
b
c
o
a
Unit Cell
Surface/ Amorphous Region
Interior/ Crystalline Region